

Scalapino<sup>18</sup>. From this one can conclude that the two components have to be comparable, as mentioned earlier. How large the ratio of the two components is has to await a more detailed analysis.

On the basis of the above discussion, it is probable that NMR  $T_2$  relaxation data integrate over the two components present in the condensate. This also appears to be the case for the recent angle-resolved photoemission experiments of Ma *et al.*<sup>19</sup> in  $\text{Bi}_2\text{Sr}_2\text{CaCu}_2\text{O}_{8+x}$ , in which the data are said to be compatible with two-component order parameter models (references to early and recent theoretical models are cited in ref. 15). In contrast, specific-heat experiments are sensitive to the presence of nodes<sup>20</sup> in the condensate, and therefore probe only the  $d$  component. The early longitudinal NMR relaxation data,  $1/T_1T$ , in YBCO-123 could be accounted for by  $d$ -symmetry<sup>21,22</sup>. But the  $T_1$  asymmetry between  $0.5 < T/T_c < 1$  is difficult to analyse in YBCO-123 (ref. 22) and in YBCO-124 (ref. 23), owing to the minimum observed in both crystals. Radio-frequency measurements on film surfaces have been interpreted more recently as proof for the existence<sup>2</sup> or absence<sup>24</sup> of nodes in the condensate.

Thus, the best recent tunnelling data in the superconducting copper oxides can be quantitatively accounted for by assuming that two order parameters of  $s$ - and  $d$ -wave symmetry are present. This assumption also involves two coherence lengths that differ by nearly an order of magnitude. Because of this difference, specific tunnelling experiments differentiate clearly between the two order parameters. As outlined above, other types of experiment either integrate or differentiate between the two components.

A certain mixing of the two components of the superconducting ground state will be present, even at low temperature,

because the cuprates do not have a tetragonal structure. This mixing will be enhanced on increasing the temperature, as the two coherence volumes in question become larger. This may account for the existence of only one  $T_c$  for the two condensates. □

Received 16 June; accepted 15 August 1995.

1. Bednorz, J. G. & Müller, K. A. *Z. Phys.* **B64**, 189–193 (1986).
2. Beasley, M. R. *IEEE Trans. Appl. Supercond.* **5**, 141–151 (1995).
3. Sun, A. G., Gajewski, D. A., Maple, M. B. & Dynes, R. C. *Phys. Rev. Lett.* **72**, 2267–2270 (1994).
4. Murakami, H., Ohbuchi, S., Hiramatsu, S. & Aoki, R. in *Proc. 6th Int. Symp. on Superconductivity, Hiroshima, Japan*, 1993 93–96 (Springer, Tokyo, 1994).
5. Wollman, D. A., Van Harlingen, D. J., Lee, W. C., Ginsberg, D. M. & Leggett, A. J. *Phys. Rev. Lett.* **71**, 2134–2137 (1993).
6. Brawner, D. A. & Ott, H. *Phys. Rev. B* (in the press).
7. Kirtley, J. R. *et al. Nature* **373**, 225–228 (1995).
8. Chaudhari, P. & Lin, S.-Y. *Phys. Rev. Lett.* **72**, 1084–1087 (1994).
9. Binning, G., Baratoff, A., Hoenig, H. E. & Bednorz, J. G. *Phys. Rev. Lett.* **45**, 1352–1355 (1980).
10. Schooly, J. F., Hosler, W. R. & Cohen, M. L. *Phys. Rev. Lett.* **12**, 474–475 (1964).
11. Kresin, V. Z. & Wolf, S. A. *Phys. Rev. B* **46**, 6438–6471 (1992).
12. Battlog, B. *Physics Today*, June, 44–50 (1991).
13. Deutscher, G. & Müller, K. A. *Phys. Rev. Lett.* **59**, 1745–1747 (1987).
14. Deutscher, G. & Simon, R. W. *J. appl. Phys.* **69**, 4137–4139 (1991).
15. Dimos, D., Chaudhari, P. & Mannhart, J. *Phys. Rev. B* **41**, 4038–4049 (1990).
16. Tsuei, C. C. *et al. Phys. Rev. Lett.* **75**, 593–596 (1994).
17. Imai, I., Slichter, C. P., Paulukas, A. P. & Veal, B. *Appl. magn. Reson.* **3**, 729–744 (1992).
18. Bulut, N. & Scalapino, D. J. *Phys. Rev. Lett.* **67**, 2898–2901 (1991).
19. Ma, J. *et al. Science* **267**, 862–865 (1995).
20. Moler, K. A. *et al. Phys. Rev. Lett.* **73**, 2744–2747 (1994).
21. Bulut, N. & Scalapino, D. J. *Phys. Rev. Lett.* **68**, 706–709 (1992).
22. Takigawa, M., Smith, J. L. & Huits, W. L. *Phys. Rev. B* **44**, 7764–7767 (1991).
23. Bankay, M., Mali, M., Roos, J., Mangelschots, I. & Brinkmann, D. *Phys. Rev. B* **46**, 11228–11231 (1992).
24. Klein, N. *et al. Phys. Rev. Lett.* **71**, 3355–3358 (1993).

ACKNOWLEDGEMENTS. I thank Hugo Keller for a critical reading and corrections of this note, which was in part written while a Regent Lecturer at UCLA and the Lawrence Berkeley Laboratory, as well as a guest of Tel Aviv University and its Sackler Institute. These stays were promoted by Vladimir Kresin and Ammon Aharony, respectively. A thorough discussion with Guy Deutscher regarding ref. 14 is especially acknowledged.

## Fully collapsed carbon nanotubes

Nasreen G. Chopra, Lorin X. Benedict,  
Vincent H. Crespi, Marvin L. Cohen,  
Steven G. Louie & A. Zettl

Department of Physics, University of California at Berkeley,  
and Materials Sciences Division, Lawrence Berkeley Laboratory,  
Berkeley, California 94720, USA

It has been suggested<sup>1</sup> that the tensile strength of carbon nanotubes<sup>2</sup> might exceed that of other known fibres because of the inherent strength of the carbon–carbon bond. Calculations of the elastic properties of nanotubes confirm that they are extremely rigid in the axial direction and are most likely to distort perpendicular to the axis<sup>3,4</sup>. Carbon nanotubes with localized kinks and bends<sup>5,6</sup>, as well as minor radial deformations<sup>7,8</sup>, have been observed. Here we report the existence of multi-shelled carbon nanotubes whose overall geometry differs radically from that of a straight, hollow cylinder. Our observations reveal nanotubes that have suffered complete collapse along their length. Theoretical modelling demonstrates that, for a given range of tube parameters, a completely collapsed nanotube is favoured energetically over the more familiar ‘inflated’ form with a circular cross-section.

Carbon nanotube samples were prepared by a carbon-arc discharge method<sup>9</sup>. Our synthesis chamber employed a water-cooled 0.625-inch graphite anode, a water-cooled copper cathode, 650 Torr of environmental helium pressure, a 120 A d.c. electrode current, and an electrode gap of a few millimetres. The carbon growth on the negative electrode was removed from the synthesis chamber and baked in flowing oxygen at 650 °C for 30 minutes to remove excess carbon particles<sup>10–12</sup>. Pieces of the baked sample were then manipulated by a glass slide and

mounted on holey carbon grids for analysis by transmission electron microscope (TEM). Samples were analysed on a JEM JEOL 200CX TEM with 200 keV accelerating voltage.

The majority of the structures imaged by TEM were consistent with previous observations: multi-walled cylindrical nanotubes with lengths varying from tens of nanometres to several micrometres, and multi-shelled ‘onions’. But we also observed long, ribbon-like structures distinctly different from conventional nanotubes. Figure 1 shows an example of such a structure, iden-

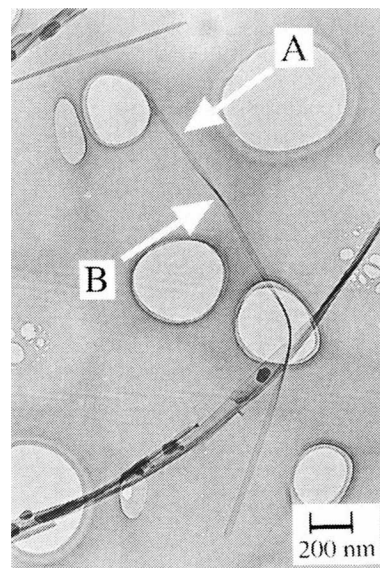


FIG. 1 TEM image of a collapsed carbon nanotube. Arrows point to flat (A) and twisted (B) regions of the collapsed tube.

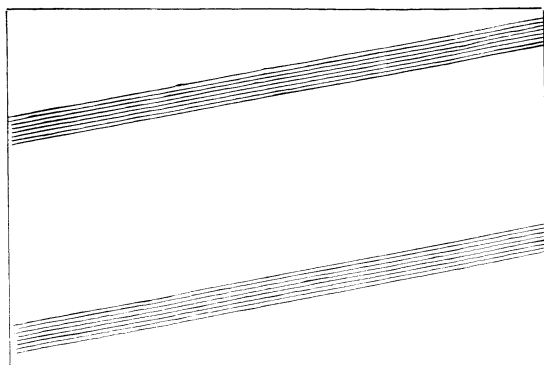
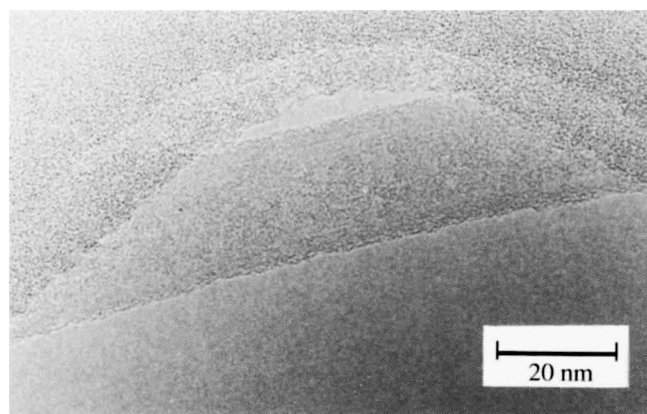


FIG. 2 High-resolution TEM image of flat region of a collapsed nanotube. The line drawing (not to scale) helps to clarify the image. Notice the equal number of lattice fringes ( $n=8$ ) on each side of gap.

tified by arrows. On initial examination, this structure looks like a flat ribbon of width 22 nm and total length 2.4  $\mu\text{m}$ , with two distinct twists along its length. A region of the structure apparently lying 'flat' against the grid substrate is marked A in the figure. One of the twists occurs over a hole in the support grid; the other twist is marked B in the figure. Other examples of such ribbon-like structures have been identified in our TEM images. We propose that these ribbon-like structures are in fact fully collapsed, flattened carbon nanotubes. We have performed additional high-resolution TEM imaging of the flat and twisted portions of several ribbon structures, and a sample rotation study, all of which support the identification of flattened tubes.

The TEM signature of a (conventional) hollow cylindrical multi-walled carbon nanotube is the observation of two parallel sets of equal-numbered lattice fringes, separated by a gap. The fringes represent the tube walls and the gap represents the hollow interior of the tube. A collapsed or flattened nanotube has a related but distinct signature. If the flat (wide) part of the tube is in the imaging plane, two parallel sets of equal-numbered lattice fringes, separated by a gap, should again be observed. If the flat part of the collapsed tube is perpendicular to the imaging plane, the number of distinct fringes should remain unchanged but the gap should be absent.

Figures 2 and 3 show this to be the case for the ribbon-like structures. Figure 2 shows a high-magnification image of the flat portion (analogous to region A in Fig. 1) of a ribbon structure different from that shown in Fig. 1. Two sets of 8 parallel lattice fringes are observed, separated by a gap of 16.2 nm. We label the inner gap width of a flattened tube as  $W_{\text{in}}$ . The full outer width of the flattened tube is  $W_{\text{out}}$ . The spacing between tube walls is calculated as about  $(W_{\text{out}} - W_{\text{in}})/(2 \times 8) \approx 3.3$  Å, consistent with the interplanar spacing of graphite (and the wall separation of conventional multi-walled nanotubes). Figure 3 shows, for the same flattened tube as in Fig. 2, a high-resolution image of a twist region. In the centre of the twist region, the flat part of the tube is perpendicular to the image plane, and here a total of 16 lattice fringes, with no gap, are observed. The greater contrast of the lattice fringes in the twist region than in the flat region is consistent with the analysis of the structure as a flat tube. The thickness  $t$  of the tube in this region is 5.3 nm ( $\sim 16 \times 3.3$  Å):  $t$  represents the 'height' of the flattened tube.

The 'twisted' regions of flattened tubes provide a convenient view of different tube orientations. However, to rule out the possibility that the ribbon structures we observe are only flattened in the twisted regions (and perhaps more like conventional, cylindrical tubes elsewhere), we performed a careful sample rotation study. The entire specimen grid was rotated *in situ* inside the TEM through angles in excess of 30°. Both ribbon structures and a 'control' conventional nanotube (located nearby on the same grid) were imaged. The control showed no change when tilted along an axis parallel to the tube axis, whereas the ribbon structure displayed a change in apparent width of the 'flat' region, consistent with a fully collapsed tube.

We have characterized a number of collapsed nanotubes in terms of number of walls  $n$  and characteristic dimensions. Table 1 summarizes the results. All collapsed tubes that we have clearly identified have  $n$  between 6 and 9, and flattened outer widths  $W_{\text{out}}$  of  $\sim 20$  nm. Table 1 also lists calculated dimensions for the inner diameter  $D_{\text{in}}$  and outer diameter  $D_{\text{out}}$  that the tube would have if it were 'inflated' and thus assumed a circular cross-section.

It is interesting to speculate how fully collapsed nanotubes come into being. It is possible that they form when a conventional hollow cylindrical nanotube is locally deformed (for example, kinked or twisted) by external mechanical forces. On kinking, the inner tube wall collapses locally and starts a zipper effect, which then flattens the tube down its entire length. The van der Waals attraction between opposing and flattened inner walls may act as an adhesive keeping the tube stable in this new position. Every fully collapsed tube that we observe contains at least one twist. This may be evidence that the twists are the origin of tube collapse. Alternatively, it may be that collapsed nanotubes are prone to twisting, much as any flat ribbon is more prone to twisting than a hollow cylindrical tube of the same material. The similarity of tube parameters for collapsed nanotubes in Table 1 suggests that a particular class of tubes is susceptible to collapse and that tubes with a greater number of walls or a smaller inner diameter than those in Table 1 have greater structural integrity.

The stability of a flat, fully collapsed nanotube may be examined with basic energetic considerations. For simplicity, consider

TABLE 1 Parameters of experimentally observed collapsed carbon nanotubes

Tube	Number of walls, $n$	$W_{\text{in}}$ (nm)	$W_{\text{out}}$ (nm)	$t$ (nm)	$D_{\text{in}}$ (nm)	$D_{\text{out}}$ (nm)	Length ( $\mu\text{m}$ )
I	9	—	22	6	10.2	16.1	2.4
II	8	15	20	5	9.5	14.8	>1.2
III	7	—	20	4.8	9.7	14.3	>1.9
IV	6	16	20	4	10.2	14.2	>0.2
V	8	16.2	21.5	5.3	10.3	15.6	3

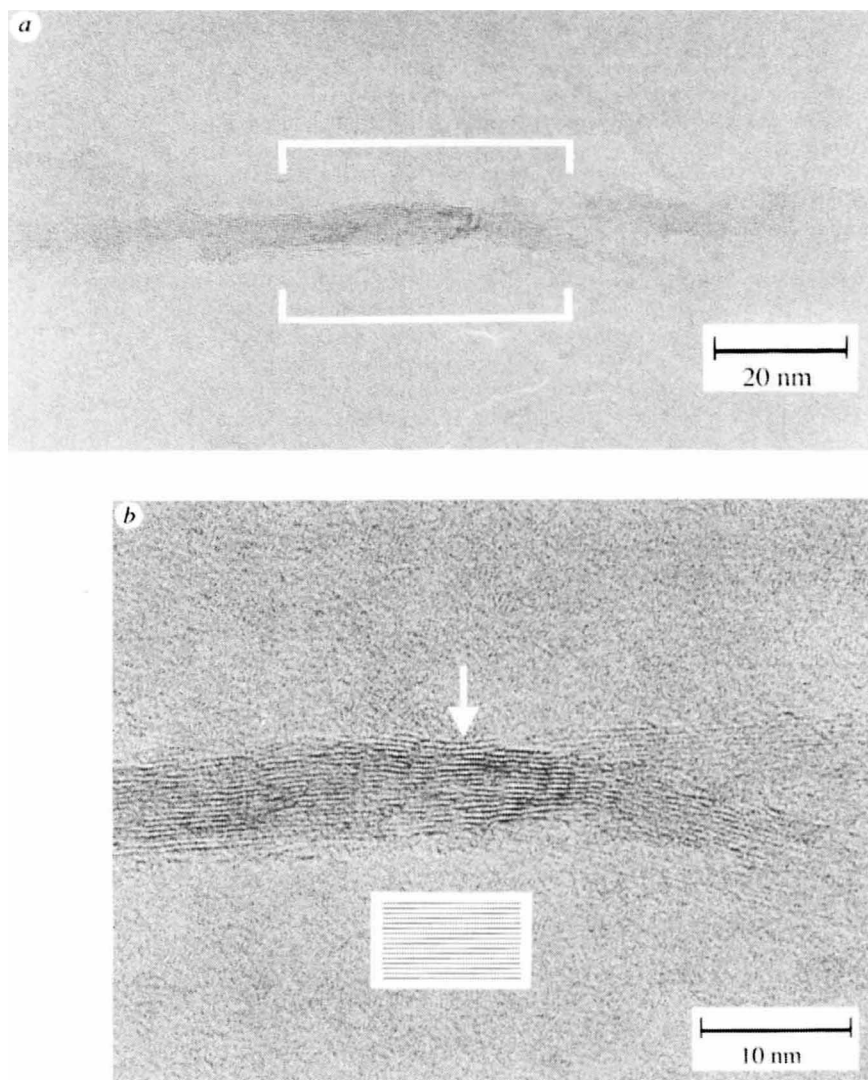


FIG. 3 *a*, High-resolution TEM image of twisted region of a collapsed nanotube. *b*, Close-up of the boxed region in *a*. Inset (not drawn to scale) points to the main feature of the collapsed tube when the flat part is perpendicular to the imaging plane, namely 16 lattice fringes with no gap (region of vertical arrow). It should be noted that details of the fringe structure (not represented in the schematic drawing) are sensitive to the focus condition and orientation of the edges of the collapsed nanotube<sup>20</sup>.

a single-wall 'inflated' nanotube of radius  $R$ . The total energy per atom relative to a flat sheet can be calculated by modelling the tube as a membrane with curvature  $1/R$  and curvature modulus  $k$ <sup>13–16</sup>. This takes into account the increase in energy due to the introduction of  $sp^3$  character bonding. The energy per

unit length of the tube is then

$$E_{\text{tube}} = k2\pi R/(2R^2) = \pi k/R \quad (1)$$

We obtain excellent quantitative agreement between the predictions of this expression and local density approximation (LDA) calculations of the total energy of carbon nanotubes<sup>17</sup> (for tubes with radii  $>2.4$  Å) when  $k = 1.4$  eV.

The flattened (that is, collapsed) version of the same tube is a two-sheeted strip of width slightly less than  $\pi R$ . The curvature is nearly zero everywhere except at the strip edges, where the curvature is very high (see Fig. 4*a*). Assume a radius of curvature at the edges of  $r \ll R$ , the curvature energy per unit length of this structure is

$$E_c = 2ka/(2r^2) = ka/r^2 \quad (2)$$

where  $a$  is the arc length of the curved region on each of the two strip edges.  $E_c$  must be greater than  $E_{\text{tube}}$  from simple geometric considerations. But the flattened tube will also have an attractive van der Waals energy if the thickness of the strip is close to  $d$ , the graphite inter-sheet spacing. This attractive energy per unit length,  $E_v$ , is proportional to the width of the straight portion:

$$E_v = -E_{\text{vdw}}(\pi R - a) \quad (3)$$

where  $E_{\text{vdw}} \sim 0.02$  eV Å<sup>-2</sup> (ref. 18). It is reasonable to assume that  $r$  and  $a$  are independent of  $R$  and only depend on  $d$  (for  $r, a \ll R$ ). This means that  $E_c$  is a constant. Examining equations 1–3, we see that there must then be a critical value of  $R$  such

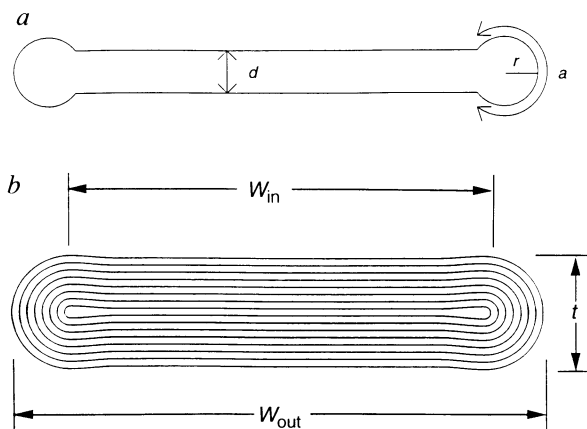


FIG. 4 *a*, Schematic cross-section of a collapsed single-wall tube:  $d$  is the interlayer distance,  $a$  is the arc length of the curved region, and  $r$  is the radius of curvature. *b*, Cross-section of theoretically modelled 8-walled fully collapsed tube with  $R = R_{\text{crit}}$ .

that for  $R < R_{\text{crit}}$ ,  $E_{\text{tube}} < E_c + E_v$  (inflated tube more favourable than collapsed tube), whereas for  $R > R_{\text{crit}}$ ,  $E_{\text{tube}} > E_c + E_v$  (collapsed tube more favourable than inflated tube).

Now consider an  $n$ -walled tube. Upon flattening, all the walls increase their curvature energy, whereas only the inner one gains attractive van der Waals energy. Thus,  $R_{\text{crit}}(n)$  is an increasing function of  $n$ . ( $R_{\text{crit}}(n)$  is the radius of the innermost wall when inflated). Using a model based on the above considerations, we have estimated (L.X.B. *et al.*, manuscript in preparation)  $R_{\text{crit}}(n)$  for several  $n$ . We find that  $R_{\text{crit}}(1) \sim 8d$ , and  $R_{\text{crit}}(8) \sim 19d$ .

Figure 4b shows our model's predicted cross-section for an  $n=8$  fully collapsed tube with  $R=R_{\text{crit}}(8)$ . For this tube,  $W_{\text{out}}$  is  $72d$  ( $=238 \text{ \AA}$ ), slightly greater than but comparable to  $W_{\text{out}} \approx 200 \text{ \AA}$  for the  $n=8$  collapsed tube observed experimentally (tubes II and V in Table 1). It must be emphasized that even if the total energy of a flattened tube is greater than that of its inflated counterpart, the flattened tube may still be metastable (that is, not prone to spontaneous 're-inflation'). We estimate that the critical radius for metastability is much less than  $R_{\text{crit}}(n)$  for each  $n$  (L.X.B. *et al.*, manuscript in preparation).

The observation of stable, flattened nanotubes may have implications for electronic and mechanical nanotube properties. For example, the electronic structure of a collapsed (carbon or other composition) nanotube may differ significantly from that of its cylindrical counterpart. Similarly, the minimum radius of curvature of bending for a flattened tube is expected to be substantially smaller for a flattened tube than for a cylindrical tube.

The interplay between curvature energy and van der Waals energy may also be relevant to the collapse of larger graphitic structures such as carbon whiskers<sup>19</sup>. □

Received 27 March; accepted 14 August 1995.

1. Ross, P. E. *Scient. Am.* **265** (December), 24 (1991).
2. Iijima, S. *Nature* **354**, 56–58 (1991).
3. Overney, G., Zhong, W. & Tomanek, D. Z. *Phys. D* **27**, 93–96 (1992).
4. Tersoff, J. & Ruoff, R. S. *Phys. Rev. Lett.* **73**, 676–679 (1994).
5. Endo, M. *et al. J. Phys. Chem. Solids* **54**, 1841–1848 (1993).
6. Despres, J. F., Daguerre, E. & Kafdi, K. *Carbon* **33**, 87–92 (1995).
7. Ruoff, R. S., Tersoff, J., Lorents, D. C., Subramoney, S. & Chan, B. *Nature* **364**, 514–516 (1993).
8. Hiura, H., Ebbesen, T. W., Fujita, J., Tanigaki, K. & Takada, T. *Nature* **367**, 148–151 (1994).
9. Kratschmer, W., Lamb, L. D., Fostiropoulos, K. & Huffman, D. R. *Nature* **347**, 354–358 (1990).
10. Ebbesen, T. W. & Ajayan, P. M. *Nature* **358**, 220–222 (1992).
11. Ebbesen, T. W., Ajayan, P. M., Hiura, H. & Tanigaki, K. *Nature* **367**, 519 (1994).
12. Colbert, D. T. *et al. Science* **266**, 1218–1222 (1994).
13. Adams, G. B., Sankey, O. F., Page, J. B., O'Keefe, M. & Drabold, D. A. *Science* **256**, 1792–1795 (1992).
14. Robertson, D. H., Brenner, D. W. & Mintmire, J. W. *Phys. Rev. B* **45**, 12592–12595 (1992).
15. Sawada, S.-I. & Hamada, N. *Solid St. Commun.* **83**, 917–919 (1992).
16. Safran, S. A. *Statistical Thermodynamics of Surfaces and Interfaces* (Addison Wesley, Reading, MA, 1994).
17. Blase, X., Rubio, A., Louie, S. G. & Cohen, M. L. *Europhys. Lett.* **28**, 335–340 (1994).
18. Girifalco, L. A. & Lad, R. A. *J. chem. Phys.* **25**, 693–697 (1956).
19. Bacon, R. J. *appl. Phys.* **31**, 283–290 (1960).
20. Iijima, S. in *Proceedings Thirty-seventh Annual Meeting Electron Microscopy Society of America* 392–395 (Claitor's, San Antonio, TX, 1979).

ACKNOWLEDGEMENTS. We thank F. Ross, C. Nelson and M. O'Keefe of the National Center for Electron Microscopy, Lawrence Berkeley Laboratory, for helpful interactions. This research was supported by the National Science Foundation, and the Director, Office of Energy Research, Office of Basic Energy Services, Materials Science Division of the U.S. Department of Energy. N.G.C. acknowledges support from a Department of Education Graduate Fellowship.

## Oxygen isotope evidence against bulk recycled sediment in the mantle sources of Pitcairn Island lavas

John M. Eiler\*, Kenneth A. Farley\*,  
John W. Valley†, Edward M. Stolper\*,  
Eric H. Hauri‡ & Harmon Craig§

\* Division of Geological and Planetary Sciences, California Institute of Technology, Pasadena, California 91125, USA

† Department of Geology and Geophysics, University of Wisconsin, Madison, Wisconsin 53706, USA

‡ Department of Terrestrial Magnetism, Carnegie Institute of Washington, 5241 Broad Branch Road, NW, Washington, DC 20015, USA

§ Scripps Institution of Oceanography, University of California San Diego, La Jolla, California 92093, USA

THE hypothesis that subducted sediments survive dehydration and/or melting in subduction zones to become long-lived geochemical reservoirs in the mantle has gained support in recent years<sup>1–3</sup>. Evidence for such reservoirs is found in the geochemistry of ocean island basalts (OIBs), some of which have isotopic and trace-element characteristics plausibly associated with ancient sedimentary components. In particular, the EM1 mantle end-member has been identified, principally on the basis of strontium, neodymium and lead isotopes, and has been proposed to carry a large sediment fraction<sup>3–5</sup>. Oxygen isotopes should be sensitive indicators of subducted sediment in the sources of OIBs because minerals that interact with water at low temperatures near the Earth's surface (during weathering, for example) become enriched in <sup>18</sup>O relative to <sup>16</sup>O (ref. 6). We report here the <sup>18</sup>O:<sup>16</sup>O ratios of phenocrysts from basalts from Pitcairn Island (southeast Pacific Ocean), which, together with the nearby Pitcairn seamounts, contain among the most extreme EM1 signatures known. We find the oxygen isotope ratios of the phenocrysts to be indistinguishable

from the average for mantle peridotite. These results show that the end-member EM1 signature can be produced in the absence of substantial (>1–2%) recycled sediment in the mantle.

Pitcairn Island basalts were collected on the 1987 *Helios* expedition of the Scripps Institution of Oceanography. Our samples are all basalts with MgO > 4 wt%. Although they were mostly collected as cobbles, they can be confidently associated with the Tedside formation of shield-building Pitcairn lavas on the basis of their chemical and isotopic characteristics (K.A.F. and E.H., unpublished results). The Sr–Nd–Pb isotopic compositions of our samples span a substantial range, up to and including the most extreme EM1 composition documented from Pitcairn Island and seamounts (Table 1 and Fig. 1).

Oxygen isotope ratios were measured at the University of Wisconsin by laser fluorination<sup>7,8</sup> of olivine, pyroxene and plagioclase phenocrysts. Results for samples and concurrently analysed garnet and olivine standards are presented in Table 1.

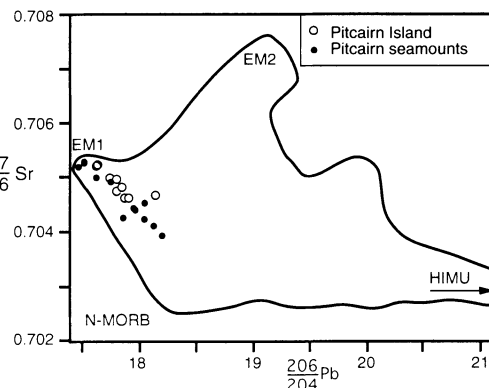


FIG. 1 Sr and Pb isotope ratios of basalts from Pitcairn Island (Tedside volcanics) and the Pitcairn seamounts (Table 1; refs 11, 18, 19). Ranges of ocean island basalts and identified mantle end-members are shown for comparison<sup>3</sup>. HIMU, N-MORB and EM2 are the radiogenic-Pb-enriched, normal MORB mantle, and enriched-mantle-2 end-members, respectively<sup>3</sup>.